

Fabrication of core-shell, yolk-shell and hollow Fe_3O_4 @carbon microboxes for high-performance lithium-ion batteries

Hao Tian,^a Hao Liu,^{b,c} Tianyu Yang,^d Jean-Pierre Veder,^e Guoxiu Wang,^c Ming Hu,^f*

Shaobin Wang,^a Mietek Jaroniec^{g} and Jian Liu^{a*}*

^a Department of Chemical Engineering, Curtin University, Perth, WA 6845, Australia.

^b School of Environmental and Chemical Engineering, Shanghai University, Shanghai, 200444

^c Centre for Clean Energy Technology, School of Mathematical and Physical Sciences, Faculty of Science, University of Technology Sydney, Broadway, Sydney, NSW 2007, Australia

^d Institute for Frontier Materials, Deakin University, Geelong, VIC 3216, Australia

^e Department of Imaging and Applied Physics, Curtin University, Perth, WA 6845, Australia

^f School of Physics and Materials Science, East China Normal University, Shanghai, 200241, China

^g Department of Chemistry and Biochemistry, Kent State University, Kent, Ohio 44242, USA

Corresponding Authors:

*Email: jian.liu@curtin.edu.au; jaroniec@kent.edu; hao.liu@uts.edu.au

EXPERIMENTAL SECTION

Cell assembly and electrochemical testing

The electrodes were prepared by mixing the active materials, carbon black (CB), and poly(vinylidene fluoride) (PVDF) used as a binder, at the weight ratio of 7:2:1. The mixture was dispersed in *n*-methyl pyrrolidone (NMP) solvent and then the slurry was uniformly pasted onto Cu foils. The electrodes were dried at 120 °C in a vacuum oven for 12 h and subsequently pressed at a pressure of 200 kg cm⁻². CR2032-type coin cells were assembled in a glove box for electrochemical measurements. A non-aqueous solution of 1 M LiPF₆ in an ethylene carbonate (EC), diethyl carbonate (DEC), and dimethyl carbonate (DMC) mixture (1:1:1) was used as the electrolyte. Li metal disks were used as the counter electrodes. The cells were galvanostatically charged and discharged in a current density range of 0.1 A g⁻¹ within the voltage range of 0.01–3.0 V. For the high rate testing, the charge/discharge current gradually increased from 0.1 to 0.2, 0.5, 1, 2, and 5 A g⁻¹ (corresponding approximately to 0.1, 0.2, 0.5, 1, 2 and 5 C, respectively), then decreased to 1 and 0.1 A g⁻¹, step by step. Cyclic voltammetry (CV) curves were collected on an electrochemistry workstation (CHI660C) at 0.1 mV s⁻¹ within a range of 0.01–3.0 V. For the electrochemical impedance spectroscopy (EIS) measurements, the excitation voltage applied to the cells was 5 mV.

Materials characterization

The sample morphology was characterized by using a transmission electron microscope (TEM, JEOL EM-2100) and a scanning electron microscope (SEM, Zeiss Neon). High Angle Annular Dark Field Scanning Transmission Electron Microscopy (HAADF-STEM) imaging and elemental mapping were carried out using a FEI Titan G2 80-200 TEM/STEM with ChemiSTEM Technology operating at 200 kV. The elemental maps were obtained by energy dispersive X-ray spectroscopy using the Super-X detector on the Titan with a probe size of ~1 nm and a probe current of ~0.4 nA. X-ray powder diffraction (XRD) analysis was performed on an X-ray diffractometer (Bruker D8 Advance) using Cu K α radiation at 40 kV and 30 mA. The BET specific surface area and single-point pore volume were obtained from nitrogen adsorption isotherms measured at -196 °C using a gas sorption instrument (Micromeritics TriStar II Surface Area and Porosity Analyzer). Prior to nitrogen adsorption measurements, the samples were degassed at 250 °C overnight. X-ray photoelectron spectroscopy (XPS) measurements were performed on a Kratos Axis Ultra DLD spectrometer using a

monochromatic AlK α (1486.6 eV) irradiation source operated at 150 W. The vacuum pressure of the analysis chamber of the spectrometer was maintained a 5×10^{-11} Torr or lower during analysis. The electron binding energy scale was calibrated for each sample by setting the main line of the C 1s spectrum to 284.5 eV. The XPS spectra were collected with a pass energy of 160 eV for the survey spectra and 40 eV for the high-resolution spectra. Data files were processed using CasaXPS software and interpreted using relative sensitivity factors provided by the instrument manufacturer (Kratos) as a guide. Background subtractions using a Shirley background were applied to all high-resolution spectra. Each high-resolution spectra were fitted with a Gaussian-Lorentzian (70%-30%) line shape with the full-width half maximum (FWHM) constrained to values considered reasonable for each element. In the case of the Fe 2p spectra, for which the interpretation of Fe oxidation states is known to be complicated by complex multiplet splitting, a simplified approach adapted from Lin et. al.¹ was used to obtain the approximate Fe²⁺/Fe³⁺ ratios. Briefly, the broad peak shapes were used to quantify Fe²⁺ and Fe³⁺ components, with the shake-up satellites used as approximate guides for the positioning of the main 2p peaks.

FIGURES

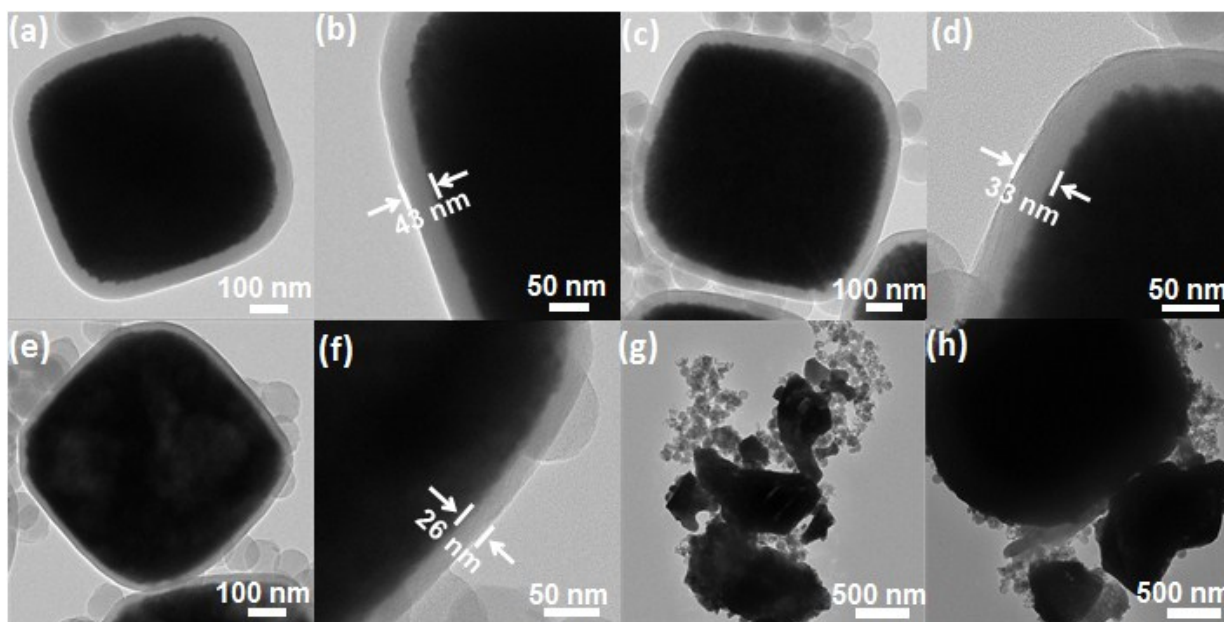


Figure S1. TEM images of FP-43 (a)(b), FC-43-500 (c)(d), FC-43-700 (e)(f) and FC-43-900 (g)(h).

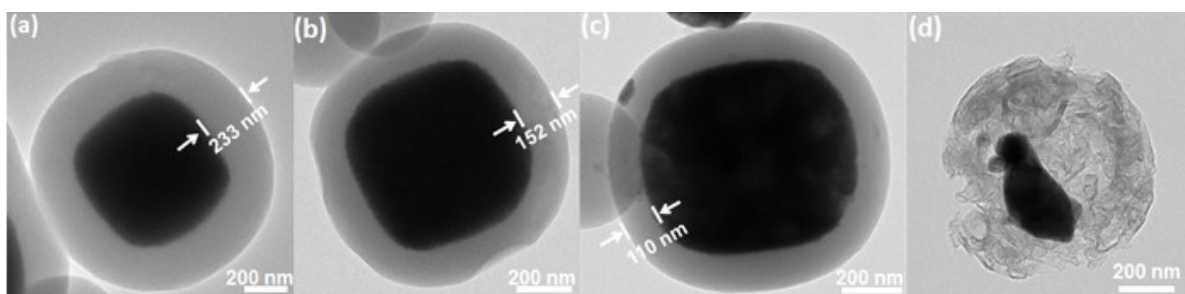


Figure S2. TEM images of FP-233 (a), FC-223-500 (b), FC-43-700 (c) and FC-43-900 (d).

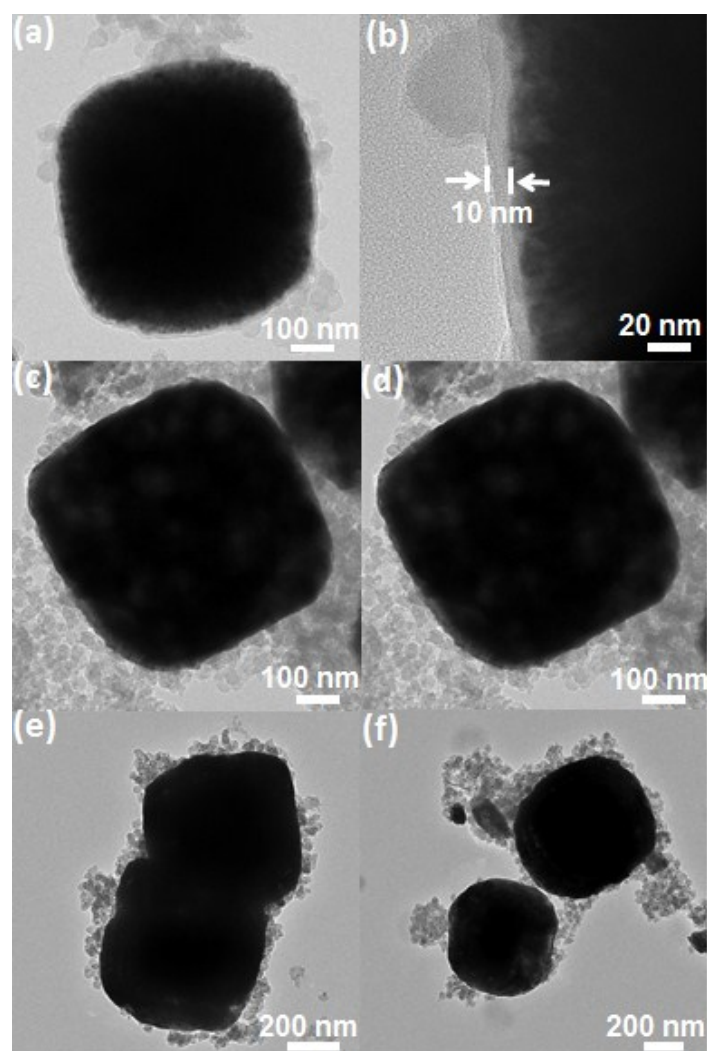


Figure S3. TEM images of FP-10 (a)(b), FC-10-500 (c)(d) and FC-10-700 (e)(f)

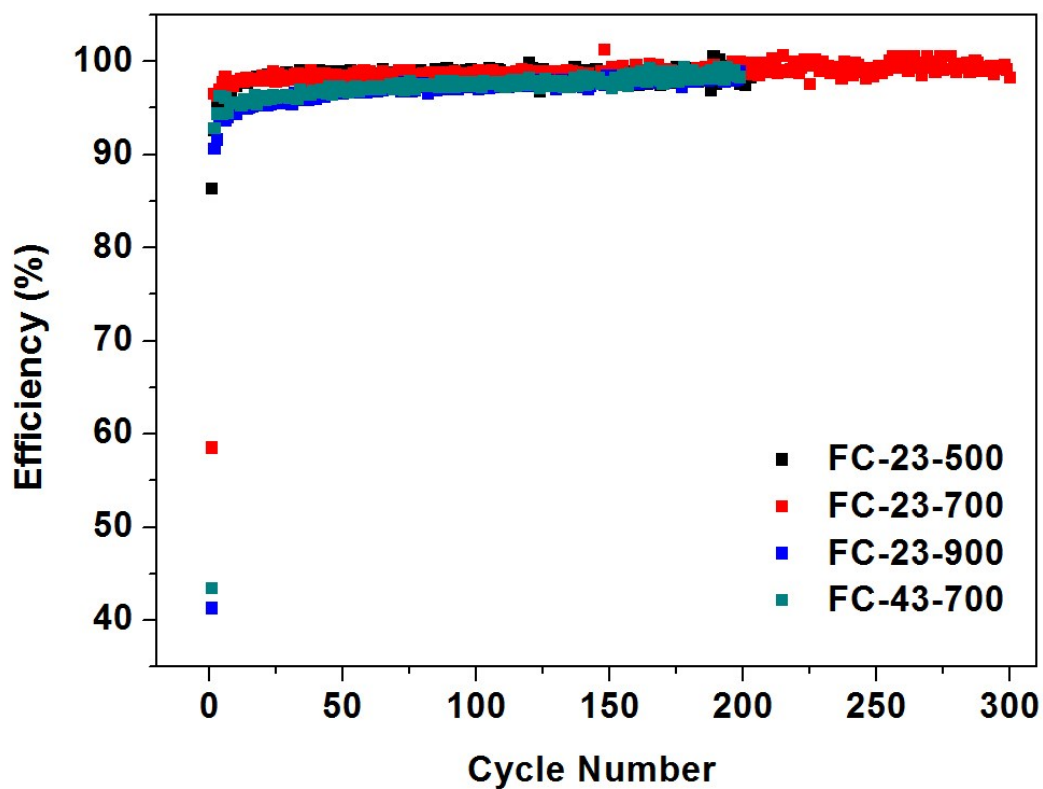


Figure S4. Coulombic efficiency curves of FC-23-500, FC-23-700, FC-23-900 and FC-43-700.

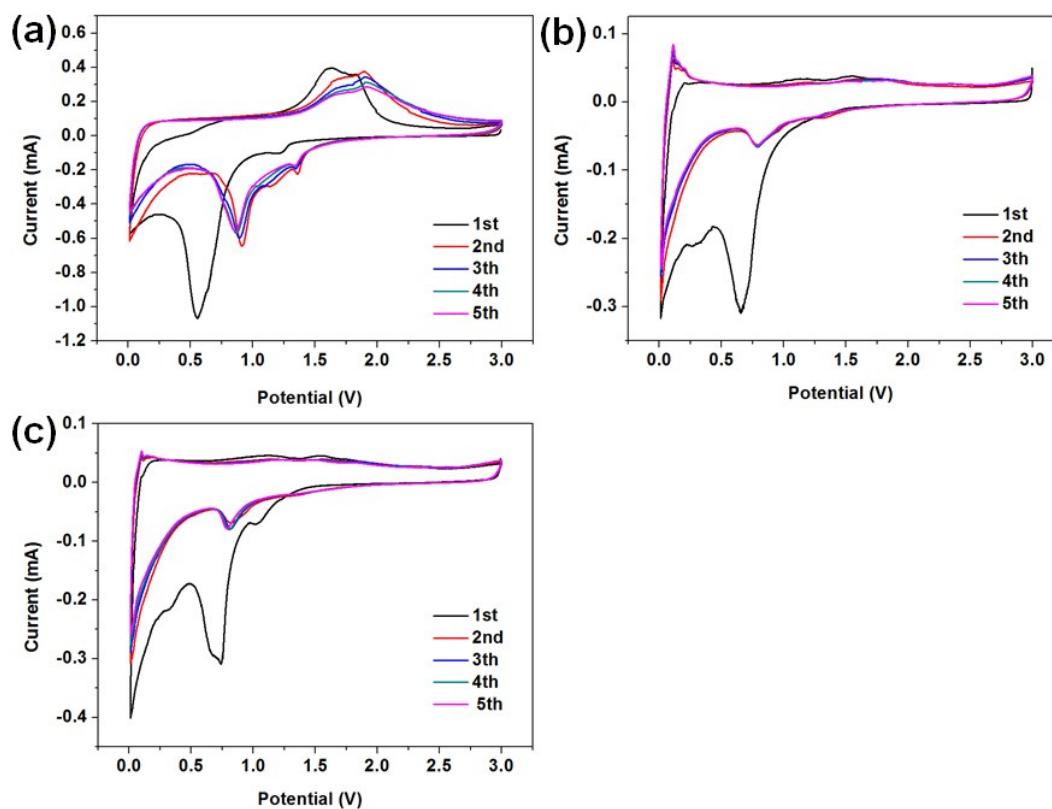


Figure S5. Cyclic voltammograms of FC-23-700 (a), FC-23-900 (b) and FC-43-700 (c) at a scan rate of 0.1 mVs⁻¹ between 0.01 and 3.0 V,

Table S1. Physical properties of FC.

Sample	BET surface area (m ² /g) ^a	Pore volume (cm ³ /g) ^b	Layer thickness (nm) ^c
FC-23-500	156	0.30	15
FC-23-700	90	0.21	12
FC-23-900	30	0.08	8
FC-43-700	184	0.35	26

^a Specific surface area was calculated by the BET method. ^b The pore volume was evaluated by using the adsorption value at P/P₀~0.99. ^c The mean layer thickness was estimated by TEM analysis.

Table S2. The chemical composition of FC-23-500, FC-23-700, FC-23-900 and FC-43-700 obtained by XPS analysis.

Sample	C (at.%)	N (at.%)	O (at.%)	Fe (at.%)
FC-23-500	81.5	7.4	11.0	0.1
FC-23-700	85.2	3.6	9.4	1.8
FC-23-900	89.1	1.1	8.0	1.8
FC-43-700	85.4	3.0	9.3	2.3

Table S3. The atomic percentage of pyridinic N, pyrrolic N, quaternary N and oxidized N in FC-23-500, FC-23-700, FC-23-900 and FC-43-700 obtained on the basis of high resolution N 1s XPS spectra.

Sample	Pyridinic N (at.%)	Pyrrolic N (at.%)	Quaternary N (at.%)	Oxidized N (at.%)
FC-23-500	27.4	31.8	27.9	13.0
FC-23-700	35.4	12.3	47.4	4.9
FC-23-900	18.1	12.9	57.7	11.3
FC-43-700	31.0	10.3	47.5	11.2

Table S4. Comparison of the structural parameters and the electrochemical performance of different Fe₃O₄-based electrode materials.

Sample name	S _{BET} (m ² /g)	V _{total} (cm ³ /g)	Reversible capacity (mAh/g)	Current density (mA/g)	Ref.
FC-23-500	156	0.30	527/100	1000	This work
H-Fe ₃ O ₄ /GS	46	-	550/50	1000	2
GNS/Fe ₃ O ₄	53	0.23	605/100	1050	3
Fe ₃ O ₄ -C	35	-	530/80	1000	4
Fe ₃ O ₄ /C composite beads	-	-	573/50	500	5
Fe ₃ O ₄ @C composites	-	-	615/50	500	6
Hollow and yolk-shell FeOx /FLG composite			335/120	1000	7
Graphene Fe ₃ O ₄ @carbon composites	-	-	570/100	1000	8

References

1. Lin, T.; Seshadri, G.; Kelber, J. A., A consistent method for quantitative XPS peak analysis of thin oxide films on clean polycrystalline iron surfaces. *Appl. Surf. Sci.* **1997**, *119* (1), 83-92.
2. Wang, R.; Xu, C.; Sun, J.; Gao, L.; Lin, C., Flexible Free-standing Hollow Fe₃O₄/graphene Hybrid Films for Lithium-ion Batteries. *J. Mater. Chem. A* **2013**, *1* (5), 1794-1800.
3. Zhou, G.; Wang, D. W.; Li, F.; Zhang, L.; Li, N.; Wu, Z.-S.; Wen, L.; Lu, G. Q.; Cheng, H. M., Graphene-Wrapped Fe₃O₄ Anode Material with Improved Reversible Capacity and Cyclic Stability for Lithium Ion Batteries. *Chem. Mater.* **2010**, *22* (18), 5306-5313.
4. Zhang, W.-M.; Wu, X.-L.; Hu, J.-S.; Guo, Y.-G.; Wan, L.-J., Carbon Coated Fe₃O₄ Nanospindles as a Superior Anode Material for Lithium-Ion Batteries. *Adv. Funct. Mater.* **2008**, *18* (24), 3941-3946.
5. Chen, Y.; Xia, H; Lu, L; Xue, J. M., Synthesis of Porous Hollow Fe₃O₄ Beads and Their Applications in Lithium Ion Batteries. *J. Mater. Chem.* **2012**, *22* (11), 5006-5012.
6. Lim, B.; Jin, J.; Yoo, J.; Han, S. Y.; Kim, K.; Kang, S.; Park, N.; Lee, S. M.; Kim, H. J.; Son, S. U., Fe₃O₄ Nanosphere@microporous Organic Networks: Enhanced Anode Performances in Lithium Ion Batteries Through Carbonization. *Chem. Commun.*, **2014**, *50* (57), 7723-7726.

7. Sun, Z. Y.; Xie, K. P.; Li, Z. A.; Sinev, I.; Ebbinghaus, P.; Erbe, A.; Farle, M.; Schuhmann, W.; Muhler, M.; Ventosa, E., Hollow and Yolk-Shell Iron Oxide Nanostructures on Few-Layer Graphene in Li-Ion Batteries. *Chem. Eur. J.* **2014**, 20 (7), 2022 – 2030.
8. Zhao, L; Gao, M. M.; Yue, W. B.; Jiang, Y.; Wang, Y.; Ren, Y.; Hu F. Q., Sandwich-Structured Graphene-Fe₃O₄@Carbon Nanocomposites for High-Performance Lithium-Ion Batteries. *ACS Appl. Mater. Interfaces.* **2015**, 7 (18), 9709–9715.